Effects of membrane and flexural stiffnesses on aortic valve dynamics: identifying the mechanics of leaflet flutter in thinner biological tissues

Emily L. Johnson[a,*], Manoj R. Rajanna[b], Cheng-Hau Yang[b], Ming-Chen Hsu[b]

[a] *Department of Aerospace and Mechanical Engineering, University of Notre Dame, Notre Dame, Indiana 46556, USA*
[b] *Department of Mechanical Engineering, Iowa State University, Ames, Iowa 50011, USA*

Abstract

Valvular pathologies that induce deterioration in the aortic valve are a common cause of heart disease among aging populations. Although there are numerous available technologies to treat valvular conditions and replicate normal aortic function by replacing the diseased valve with a bioprosthetic implant, many of these devices face challenges in terms of long-term durability. One such phenomenon that may exacerbate valve deterioration and induce undesirable hemodynamic effects in the aorta is leaflet flutter, which is characterized by oscillatory motion in the biological tissues. While this behavior has been observed for thinner bioprosthetic valves, the specific underlying mechanics that lead to leaflet flutter have not previously been identified. This work proposes a computational approach to isolate the fundamental mechanics that induce leaflet flutter in thinner biological tissues during the cardiac cycle. The simulations in this work identify reduced flexural stiffness as the primary factor that contributes to increased leaflet flutter in thinner biological tissues, while decreased membrane stiffness and mass of the thinner tissues do not directly induce flutter in these valves. The results of this study provide an improved understanding of the mechanical tissue properties that contribute to flutter and offer significant insights into possible developments in the design of bioprosthetic tissues to account for and reduce the incidence of flutter.

Keywords: Heart valve; Leaflet flutter; Membrane and flexural stiffnesses; Fluid–structure interaction; Isogeometric Kirchhoff–Love shell

---

1. Introduction

The high prevalence of aortic valve diseases among aging populations has driven developments in valvular treatment technologies, including surgical bioprosthetic heart valves [1] and transcatheter valve replacement procedures [2, 3], which have both become increasingly common options to restore proper cardiac function [4]. Compared to mechanical valves, bioprosthetic technologies offer a more suitable option to replicate the overall structure and performance of native heart valves [5]. However, given that surgical operations to replace the aortic valve with a bioprosthesis require high-risk, invasive procedures that often involve long post-operative recovery times, the introduction of percutaneous valve replacement technologies has provided a strong alternative to surgical implant operations in the treatment of aortic valve diseases [6, 7].

Although bioprosthetic valves and transcatheter implant technologies have become relatively mature in recent years, numerous issues remain in improving the safety of catheter-based deployment approaches and the durability of the biological tissues. One practical design approach to reduce the risk of complications during percutaneous valve implant operations is to use prosthetic devices that incorporate thinner leaflet tissues and can be deployed through smaller-diameter catheters [8]. While this approach is effective for the deployment of transcatheter devices, thinner tissues have also been associated with flutter in the heart valve leaflets [9]. The induced oscillations in tissues with reduced thickness can cause disturbances and other abnormal fluid phenomena in the blood flow that may lead to thrombus or embolus formation [10–12]. In addition to the problematic hemodynamic behaviors resulting from flutter, the high-frequency cyclic loading in tissues that exhibit flutter may also accelerate other mechanical issues, such as deterioration, reduced durability, and fatigue in bioprosthetic valve implants [13–17], which are already susceptible to calcification, leaflet tears and perforations, and other types of failure [18–22].

While it is clear that thinner tissues can induce leaflet flutter in heart valves, the underlying mechanics that contribute to this phenomenon have not been specifically identified. For these tissues, three primary aspects of the structure are impacted when the thickness is altered: membrane stiffness, flexural stiffness, and mass. Based on classical plate theory, in which the membrane stiffness exhibits linear variation with thickness while the bending stiffness exhibits cubic variation with thickness [23], one may postulate that the reduced bending stiffness introduces the most significant contribution to the flutter instability [24]; however, the specific impact of the different tissue mechanics on the flutter behavior of bioprosthetic valves has not been directly isolated. For example, it is not clear how reducing the membrane and flexural stiffnesses contributes to leaflet flutter.

---

[*] Corresponding author
Email addresses: `eljohnson@nd.edu` (Emily L. Johnson), `jmchsu@iastate.edu` (Ming-Chen Hsu)

The final publication is available at Elsevier via https://doi.org/10.1016/j.finmec.2021.100053

In order to differentiate the fundamental mechanics that lead to flutter phenomena in heart valves with thinner leaflet tissues, this work proposes a simulation-based approach to identify the impact of individual tissue characteristics. The computational methods proposed in this work enable a decoupled approach to directly isolate the contribution of the membrane stiffness, flexural stiffness, and mass to the flutter of heart valve leaflets that comprise thinner tissues. Using the proposed framework, which incorporates an immersogeometric analysis (IMGA) approach for fluid–structure interaction (FSI) analysis of heart valves [25, 26], the effect of these quantities on the flow behavior, valve dynamics, and induced flutter response are investigated throughout the entire cardiac cycle.

This paper is organized into the following parts. Section 2 describes the IMGA FSI simulation framework, the details of the approach for isolating the membrane and flexural stiffnesses, and the computational setup for the valve. Section 3 presents the FSI simulation results and quantities of interest related to the blood flow and leaflets for five different valve cases. Discussion and conclusions on the effects of the leaflet mass, membrane stiffness, and flexural stiffness on the cardiac system are presented in Section 4.

2. Material and Methods

2.1. Fluid–structure interaction methodology

The heart valve simulations in this study are performed using the IMGA FSI framework [25–33]. This methodology incorporates a hybrid approach for modeling different parts of the overall FSI problem with either a traditional boundary-fitted method [34, 35] or an immersed approach [25, 36] depending which is more practical for the specific subproblem. For FSI problems that involve large structural deformation or changes in the fluid domain topology, the immersed approach provides significant geometric flexibility and offers many advantages over traditional boundary-fitted FSI methods. For the simulations in this study, the heart valve is immersed into the non-boundary-fitted discretization of the background fluid mesh to flexibly simulate the large deformations that are present in this FSI problem, and the artery wall and the blood-flow domain are boundary-fitted and conforming. The flow is governed by the Navier–Stokes equations of incompressible flows, which are discretized using a variational multiscale (VMS) method [37–39] and solved on an arbitrary Lagrangian–Eulerian (ALE) frame [40]. The ALE formulation is a suitable approach for moving domain simulations, such as the deforming-artery blood-flow problem in this work, and the VMS method inherently includes a large-eddy simulation turbulence model that is effective for modeling the possibly turbulent blood flow in the near-valve region of the aorta.

The artery wall is modeled as a large-deformation hyperelastic solid that is written in a Lagrangian frame [41]. As will be discussed in further detail in the following sections, the heart valve leaflets are modeled as thin-shell structures using a hyperelastic Kirchhoff–Love shell formulation [42, 43]. The conforming discretization that is employed between the artery and the blood-flow domain ensures that the kinematic- and traction-compatibility conditions are automatically satisfied and that the FSI coupling is handled using a monolithic formulation [41]. The IMGA approach is used to directly analyze the spline-based representations of the valve structures, where a dynamic augmented Lagrangian method [26] is applied to weakly enforce constraints at the immersed interface between the fluid and shell structure components in the valvular FSI analysis. A penalty-based method is applied to enforce contact between shell structures during the valve closure [25]. The combination of these various components comprises the IMGA FSI framework, which is discretized in time using the generalized-α method [41]. Detailed discussions and formulations of the methods that are employed in the IMGA FSI framework can be found in the aforementioned references.

2.2. Shell structural formulation

The thin-tissue structures of the leaflets are modeled as hyperelastic isogeometric Kirchhoff–Love shells [42, 43]. In Kirchhoff–Love shell theory, both normal and transverse shear strains are neglected, and only the in-plane strain components are considered. Within this formulation, a point $\mathbf{x}$ in the shell continuum can be described by a point $\mathbf{r}$ on the midsurface and a vector $\mathbf{a}_3$ normal to the midsurface:

$$\mathbf{x}(\xi^1,\xi^2,\xi^3) = \mathbf{r}(\xi^1,\xi^2) + \xi^3\,\mathbf{a}_3(\xi^1,\xi^2)\,, \tag{1}$$

where ξ^1, ξ^2 are the contravariant coordinates of the midsurface, $\xi^3 \in [-h/2, h/2]$ is the through-thickness coordinate, and h is the shell thickness. The Green–Lagrange strain $\mathbf{E}$ is assumed to vary linearly through the shell thickness and can be expressed as a combination of the midsurface membrane strain and the through-thickness bending strain. For the formulations in this section, let Greek indices take values of 1 or 2 to denote the in-plane components. The covariant components of $\mathbf{E}$ can be obtained as

$$E_{\alpha\beta} = \varepsilon_{\alpha\beta} + \xi^3 \kappa_{\alpha\beta}\,, \tag{2}$$

where $\varepsilon_{\alpha\beta}$ and $\kappa_{\alpha\beta}$ are the covariant components of the membrane strain tensor, $\boldsymbol{\varepsilon}$, and curvature change (due to bending) tensor, $\boldsymbol{\kappa}$, of the midsurface, respectively.

The weak form of the shell formulation is defined as

$$\int_{\mathcal{S}_0} \mathbf{w}\cdot\rho h \frac{\mathrm{d}^2\mathbf{y}}{\mathrm{d}t^2}\,\mathrm{d}\mathcal{S} + \int_{\mathcal{S}_0}\int_{-h/2}^{h/2} \delta\mathbf{E} : \mathbf{S}\,\mathrm{d}\xi^3\mathrm{d}\mathcal{S} - \int_{\mathcal{S}_0} \mathbf{w}\cdot\rho h\mathbf{f}\,\mathrm{d}\mathcal{S} - \int_{\mathcal{S}_t} \mathbf{w}\cdot\mathbf{h}\,\mathrm{d}\mathcal{S} = 0\,, \tag{3}$$

where $\mathcal{S}_0$ and $\mathcal{S}_t$ are the shell midsurfaces in the reference and deformed configurations, respectively, $\mathbf{y}$ is the midsurface displacement, $\mathrm{d}(\cdot)/\mathrm{d}t$ is defined as a time derivative that is taken while holding the material coordinate fixed, ρ is the shell density, $\delta\mathbf{E}$ is the variation of $\mathbf{E}$ corresponding to displacement variation $\mathbf{w}$, $\mathbf{S}$ is the second Piola–Kirchhoff stress tensor obtained from a hyperelastic strain energy density functional ψ, $\mathbf{f}$ is a prescribed body force, and $\mathbf{h}$ is the total traction from the two sides of the shell.

In hyperelastic shell analysis, one can linearize and derive an in-plane material tangent tensor $\hat{\mathbb{C}}$ [42, Eq. (39)] based on the plane stress condition such that

$$\mathrm{d}S^{\alpha\beta} = \hat{\mathbb{C}}^{\alpha\beta\gamma\delta}\mathrm{d}E_{\gamma\delta}\,, \tag{4}$$

where d**S** and d**E** are total differentials of **S** and **E**. Note that $\hat{\mathbb{C}}$ can vary through the shell thickness. The stress resultants, obtained by integration through the thickness, are defined as

$$\mathbf{n} = \int_{-h/2}^{h/2} \mathbf{S}\,\mathrm{d}\xi^3\,, \tag{5}$$

$$\mathbf{m} = \int_{-h/2}^{h/2} \mathbf{S}\,\xi^3\mathrm{d}\xi^3\,, \tag{6}$$

where **n** is the normal force and **m** is the bending moment. For their total differentials, according to Eqs. (2) and (4), we obtain

$$\mathrm{d}\mathbf{n} = \left(\int_{-h/2}^{h/2} \hat{\mathbb{C}}\,\mathrm{d}\xi^3\right)\mathrm{d}\boldsymbol{\varepsilon} + \left(\int_{-h/2}^{h/2} \hat{\mathbb{C}}\,\xi^3\mathrm{d}\xi^3\right)\mathrm{d}\boldsymbol{\kappa}\,, \tag{7}$$

$$\mathrm{d}\mathbf{m} = \left(\int_{-h/2}^{h/2} \hat{\mathbb{C}}\,\xi^3\mathrm{d}\xi^3\right)\mathrm{d}\boldsymbol{\varepsilon} + \left(\int_{-h/2}^{h/2} \hat{\mathbb{C}}\left(\xi^3\right)^2\mathrm{d}\xi^3\right)\mathrm{d}\boldsymbol{\kappa}\,. \tag{8}$$

Based on Eq. (3), the internal virtual work can be defined as

$$\delta W^{\text{int}} = \int_{\mathcal{S}_0} \left(\mathbf{n} : \delta\boldsymbol{\varepsilon} + \mathbf{m} : \delta\boldsymbol{\kappa}\right)\mathrm{d}\mathcal{S}\,, \tag{9}$$

which can be linearized to obtain the internal nodal forces $\mathbf{F}^{\text{int}}$ and stiffness matrix $\mathbf{K}^{\text{int}}$ by taking derivatives of Eq. (9) with respect to the displacement variables [23, 42]:

$$F_r^{\text{int}} = \frac{\partial W^{\text{int}}}{\partial u_r} = \int_{\mathcal{S}_0}\left(\mathbf{n} : \frac{\partial\boldsymbol{\varepsilon}}{\partial u_r} + \mathbf{m} : \frac{\partial\boldsymbol{\kappa}}{\partial u_r}\right)\mathrm{d}\mathcal{S}\,, \tag{10}$$

$$\begin{aligned} K_{rs}^{\text{int}} &= \frac{\partial^2 W^{\text{int}}}{\partial u_r \partial u_s} \\ &= \int_{\mathcal{S}_0}\Bigg(\left(\mathbb{D}_A\frac{\partial\boldsymbol{\varepsilon}}{\partial u_s} + \mathbb{D}_B\frac{\partial\boldsymbol{\kappa}}{\partial u_s}\right) : \frac{\partial\boldsymbol{\varepsilon}}{\partial u_r} + \mathbf{n} : \frac{\partial^2\boldsymbol{\varepsilon}}{\partial u_r\partial u_s} \\ &\quad + \left(\mathbb{D}_B\frac{\partial\boldsymbol{\varepsilon}}{\partial u_s} + \mathbb{D}_D\frac{\partial\boldsymbol{\kappa}}{\partial u_s}\right) : \frac{\partial\boldsymbol{\kappa}}{\partial u_r} + \mathbf{m} : \frac{\partial^2\boldsymbol{\kappa}}{\partial u_r\partial u_s}\Bigg)\mathrm{d}\mathcal{S}\,, \end{aligned} \tag{11}$$

where r and s are the indices for the total degrees of freedom of the system, u_r and u_s are the discrete nodal displacements, and

$$\mathbb{D}_A = \int_{-h/2}^{h/2} \hat{\mathbb{C}}\,\mathrm{d}\xi^3\,, \tag{12}$$

$$\mathbb{D}_B = \int_{-h/2}^{h/2} \hat{\mathbb{C}}\,\xi^3\mathrm{d}\xi^3\,, \tag{13}$$

$$\mathbb{D}_D = \int_{-h/2}^{h/2} \hat{\mathbb{C}}\left(\xi^3\right)^2\mathrm{d}\xi^3\,. \tag{14}$$

In Eq. (11), the terms associated with $\mathbb{D}_{(\cdot)}$ are the material stiffness contributions and the terms associated with **n** and **m** are the geometric stiffness contributions to the internal stiffness, which can be broken down into membrane, bending, and membrane–bending coupling stiffnesses. In this work, the flexural stiffness is defined as the combination of the latter two.

2.3. Isolating membrane and flexural stiffnesses

The intent of this work is to investigate the individual impact of a reduced membrane or flexural stiffness (e.g., due to reduced thickness) on leaflet flutter. This requires isolating the change of membrane or flexural stiffness due to a change of thickness in Eq. (11). However, this is not a trivial task. In the case of St. Venant–Kirchhoff material, which assumes a linear stress–strain relationship, it is relatively simple to separate Eq. (11) into membrane and bending contributions (see Appendix A).[1] However, in the case of general hyperelastic materials, because **S** and $\hat{\mathbb{C}}$ are generally obtained based on the derivatives of ψ with respect to **E** (see [42] for details), it is not straightforward to isolate the membrane and flexural contributions in Eq. (11). For example, **S**, and as a result, **n**, inherently has contributions associated with $\boldsymbol{\kappa}$ that can not be easily isolated for general hyperelastic materials.

To overcome this issue, a novel approach based on a one-point quadrature scheme for the through-thickness integration is proposed for the evaluation of the internal stiffness terms. This approach offers an effective strategy to isolate the membrane stiffness and avoid discrepancies with the flexural stiffness terms. When one-point quadrature is employed for the through-thickness integration, the integrands are evaluated at a single integration point at the midsurface location ($\xi^3 = 0$). In the application of this strategy, Eqs. (5), (6), and (12)–(14) become the following:

$$\widetilde{\mathbf{n}} = h\,\mathbf{S}|_{\xi^3=0}\,, \tag{15}$$

$$\widetilde{\mathbf{m}} = 0\,, \tag{16}$$

$$\widetilde{\mathbb{D}}_A = h\,\hat{\mathbb{C}}|_{\xi^3=0}\,, \tag{17}$$

$$\widetilde{\mathbb{D}}_B = 0\,, \tag{18}$$

$$\widetilde{\mathbb{D}}_D = 0\,, \tag{19}$$

where $\widetilde{(\cdot)}$ indicates variables integrated with one-point quadrature along the thickness direction. Based on these updated quantities, the internal stiffness matrix evaluated using one-point quadrature through the thickness reduces to

$$\widetilde{K}_{rs}^{\text{int}} = \int_{\mathcal{S}_0}\left(\widetilde{\mathbb{D}}_A\frac{\partial\boldsymbol{\varepsilon}}{\partial u_s} : \frac{\partial\boldsymbol{\varepsilon}}{\partial u_r} + \widetilde{\mathbf{n}} : \frac{\partial^2\boldsymbol{\varepsilon}}{\partial u_r\partial u_s}\right)\mathrm{d}\mathcal{S}\,, \tag{20}$$

which only contains contributions related to the membrane stiffness. In using this approach to decouple and isolate the components of the internal stiffness that are individually related to either the membrane or flexural stiffness, the follow matrix definitions are adopted. $\mathbf{K}_{1.0}^{\text{int}}$ and $\mathbf{K}_{0.5}^{\text{int}}$ are the stiffness matrices calculated based on $h = 1.0H$ and $h = 0.5H$, respectively, where H is the baseline shell thickness and h is the shell thickness

---

[1] For the St. Venant–Kirchhoff material, note that the coupling stiffness is zero, and the flexural stiffness includes only bending contributions.

used in the through-thickness integration. $\widetilde{\mathbf{K}}^{\text{int}}_{1.0}$ and $\widetilde{\mathbf{K}}^{\text{int}}_{0.5}$ are the stiffness matrices computed based on the one-point quadrature definition for the corresponding shell thicknesses. We then define

$$\mathbf{K}^{\text{me}}_{1.0} = \widetilde{\mathbf{K}}^{\text{int}}_{1.0} \, , \tag{21}$$

$$\mathbf{K}^{\text{fle}}_{1.0} = \mathbf{K}^{\text{int}}_{1.0} - \widetilde{\mathbf{K}}^{\text{int}}_{1.0} \, , \tag{22}$$

$$\mathbf{K}^{\text{me}}_{0.5} = \widetilde{\mathbf{K}}^{\text{int}}_{0.5} \, , \tag{23}$$

$$\mathbf{K}^{\text{fle}}_{0.5} = \mathbf{K}^{\text{int}}_{0.5} - \widetilde{\mathbf{K}}^{\text{int}}_{0.5} \, , \tag{24}$$

where $\mathbf{K}^{\text{me}}_{(\cdot)}$ and $\mathbf{K}^{\text{fle}}_{(\cdot)}$ indicate the membrane and flexural stiffnesses, respectively. For each case in which a different membrane or flexural stiffness contribution is incorporated, the corresponding internal stiffness can be computed by combining the contributions from each individual stiffness matrix. For example, in a case with 50% reduced membrane stiffness and baseline flexural stiffness, the internal stiffness can be computed as

$$\mathbf{K}^{\text{me}}_{0.5} + \mathbf{K}^{\text{fle}}_{1.0} = \left(\widetilde{\mathbf{K}}^{\text{int}}_{0.5}\right) + \left(\mathbf{K}^{\text{int}}_{1.0} - \widetilde{\mathbf{K}}^{\text{int}}_{1.0}\right) \, . \tag{25}$$

2.4. *Simulation setup*

The computational setup for the heart valve simulations is shown in Fig. 1. We refer to the "inlet" as the left ventricular end of the aorta and the "outlet" as the end of the tubular ascending aorta. An idealized left-ventricular pressure waveform is applied as a traction boundary condition at the inlet boundary of the fluid domain (not including the fluid–solid interface.) This idealized pressure waveform is selected to remove the possibility of flutter initiation due to an oscillatory pressure condition. The applied pressure signal is periodic, with a period of 0.86 s for one cardiac cycle. A resistance boundary condition [44] is applied at the outlet boundary of the fluid domain in the form of a traction $-(p_0 + RQ)\mathbf{n}_{\text{f}}$, where $p_0 = 80$ mmHg is a constant physiological pressure, $\mathbf{n}_{\text{f}}$ is the outward-facing normal vector of the fluid domain, $R = 70$ (dyn s)/cm^5 is a resistance coefficient, and Q is the outlet volumetric flow rate. Backflow stabilizations [45] are enforced at both ends of the fluid domain.

Based on previous FSI simulations of the valve [27, 28], the fluid density and dynamic viscosity are 1.0 g/cm^3 and 3.0×10^{-2} g/(cm s), respectively, which models human blood. The material for the artery wall tissue is modeled as a generalized neo-Hookean model with dilatational penalty [46] with a Young's modulus of 1.0×10^7 dyn/cm^2 and Poisson's ratio of 0.45. The density of the arterial wall is 1.0 g/cm^3, and a mass-proportional damping with coefficient 1.0×10^4 s^{-1} is added to the wall motion to model the interaction of the artery with the surrounding tissues and interstitial fluid. A zero-traction boundary condition is applied on the outer wall of the artery, and the cross sections of the inlet and outlet are allowed to slide in their respective tangential planes and deform radially, but constrained in their normal directions [47].

Following the previous flutter study [9], the valve dimensions are determined for the 23-mm-diameter annulus aorta geometry, and a typical 23-mm valve geometry is constructed with a leaflet diameter of 21.9 mm and a leaflet height of 11.1 mm (Fig. 1). While this work is motivated by transcatheter valve technologies, it primarily focuses on the mechanics of the bioprosthetic valve tissues. To investigate these fundamental characteristics, a relatively simple valve configuration is selected for this study to limit the number of additional system complexities introduced by typical percutaneous implants [32]. The stent of the bioprosthetic valve is assumed to be rigid and stationary given its large stiffness relative to the leaflets and the artery wall. Each leaflet is clamped to the stent at the attachment edge, and the entire valve is immersed into the sinus section of the aorta (sinus of Valsalva), with the suture ring of the stent intersecting the artery wall. The degrees of freedom associated with solid elements of the artery wall that are intersected by the stent are fixed in space and time. The leaflets are modeled with the transversely isotropic Lee–Sacks material model [43] with a 45° fiber orientation that approximates the collagen fiber alignment of typical pericardial tissue. The material coefficients reported by Wu et al. [43], which are obtained from fitting the equibiaxial experimental data of a glutaraldehyde-treated

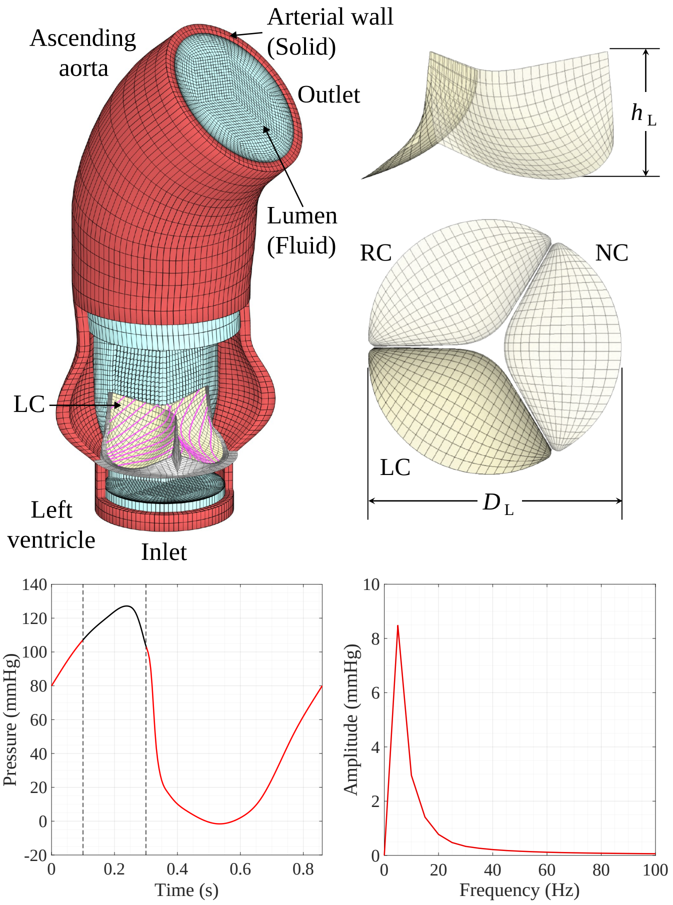

Figure 1: Setup for the FSI simulation, including the aorta model with the stress-free state of the bioprosthetic heart valves, the left ventricular pressure waveform enforced on the inlet, and the frequency analysis for the pressure signal, analyzed over the $t = 0.1$ to 0.3 s time period. The fiber orientation of 45° is shown on the leaflets in the aorta model. The valve dimensions are $D_{\text{L}} = 21.9$ mm and $h_{\text{L}} = 11.1$ mm, and the leaflets are labeled as RC: right coronary leaflet, LC: left coronary leaflet, and NC: non-coronary leaflet. The normal vectors of the leaflet surfaces point from the aortic side to the ventricular side of the valve.

bovine pericardium specimen [48], are adopted. The density of the leaflets is 1.0 g/cm^3, and the baseline leaflet thickness H is 0.368 mm.

The aorta domain is discretized with quadratic trivariate nonuniform rational B-spline elements, with 8640 elements in the artery wall and 88,560 elements in the fluid domain. The valve is modeled using cubic B-spline surfaces, with each leaflet comprising 351 B-spline elements and the stent comprising 1380 B-spline elements. The FSI simulation starts at $t = 0.6$ s, which corresponds to the diastolic phase of the cardiac cycle, with homogeneous initial conditions. The simulation advances in time using a time step size of 1.0×10^{-4}. After the initial transient from $t = 0.6$ to 0.86 s, four consecutive cardiac cycles are subsequently simulated, and the solutions from the last cardiac cycle are analyzed and reported in the following sections.

3. Results

3.1. Valve cases

To examine the effect of the membrane and flexural stiffnesses, five different valve cases are simulated and analyzed. In the previous study on the impact of tissues thickness on leaflet flutter [9], FSI simulations were carried for four different leaflet thicknesses at 100%, 75%, 50%, and 25% of the baseline tissue thickness of 0.386 mm, where the labels BP-100, BP-75, BP-50, and BP-25 were used to indicate a bovine pericardium (BP) valve at a specific percentage of the baseline thickness. Based on the results from the previous work, which indicated that flutter is not present in the BP-100 and BP-75 cases and develops in the BP-50 case, the present study primarily isolates and focuses on the BP-50 case to examine the underlying mechanics related to a reduced tissue thickness that contribute to the appearance of the flutter response.

As shown in Table 1, in addition to the baseline BP-100 case that does not induce flutter, four other valve cases are also examined. The first two additional cases, labeled as BP-M50 and BP-F50, isolate the impact of individually reducing the valve membrane and flexural stiffnesses, respectively, by computing the corresponding stiffness for a tissue thickness of 0.5H. The third case, labeled as BP-MF50, isolates the impact of simultaneously reducing the membrane and flexural stiffnesses based on 0.5H and maintaining the original mass that is consistent with a tissue thickness of 1.0H. Finally, the fourth additional case, labeled as BP-M12.5, identifies the impact of the membrane stiffness when it is reduced by a similar ratio as the flexural stiffness in the BP-F50 and BP-MF50 cases. In classical plate theory, bending stiffness varies with h^3, and a 50% thickness reduction results in a 87.5% reduction of the bending stiffness. Evaluating the membrane stiffness based on a 12.5% thickness approximates same ratio of reduction in membrane stiffness due to its proportional variation with h. For quantities reported on a single leaflet, the results are based on the data from the left coronary leaflet.

Remark 1. Based on the results for the BP-MF50 case that will be presented in the following sections, which exhibit equivalent behavior and flutter response to the original BP-50 case in Johnson et al. [9], we conclude that the mass has a negligible impact on the flutter behavior of the leaflets. After examining the impact of simultaneously reducing the membrane stiffness and mass based on the 12.5% thickness, as shown in Appendix B, the same conclusion can be drawn from the results. This additional case exhibits a very similar dynamic leaflet response as the BP-M12.5 case, so the corresponding quantities of interest for the reduced mass cases are not included in the following study.

Table 1: Valve cases for the study of membrane and flexural stiffnesses. The table shows the corresponding thickness from which the stiffness is computed for both the membrane and flexural contributions. The calculation of the stiffness matrices is based on the proposed method outlined in Section 2.3.

Valve case labels	Membrane contribution	Flexural contribution	Stiffness calculation
BP-100	1.0H	1.0H	$\mathbf{K}^{\mathrm{me}}_{1.0} + \mathbf{K}^{\mathrm{fle}}_{1.0}$
BP-M50	0.5H	1.0H	$\mathbf{K}^{\mathrm{me}}_{0.5} + \mathbf{K}^{\mathrm{fle}}_{1.0}$
BP-M12.5	0.125H	1.0H	$\mathbf{K}^{\mathrm{me}}_{0.125} + \mathbf{K}^{\mathrm{fle}}_{1.0}$
BP-F50	1.0H	0.5H	$\mathbf{K}^{\mathrm{me}}_{1.0} + \mathbf{K}^{\mathrm{fle}}_{0.5}$
BP-MF50	0.5H	0.5H	$\mathbf{K}^{\mathrm{me}}_{0.5} + \mathbf{K}^{\mathrm{fle}}_{0.5}$

3.2. Flow results

The results for the volume rendering visualization of the flow speeds and the vorticity isosurfaces, colored by the axial (normal to the aortic annulus) velocity are shown in Fig. 2 at the peak opening of the valve ($t = 0.25$ s). The transvalvular pressure gradient is also evaluated for each case as the difference between the left-ventricular pressure (0.1 cm below the annulus) and the aortic pressure (1.3 cm above the annulus) and shown in Fig. 3. As observed from the flow visualization, there are large, uninterrupted regions of high-speed flow in the aorta in the BP-100, BP-M50, and BP-M12.5 cases and relatively minimal vortex formation near the leaflets. The BP-F50 and BP-MF50 cases exhibit more chaotic, disturbed flow in the downstream region and additional vortices induced near the heart valve, which were previously identified as typical characteristics of valves that experience leaflet flutter [9].

When evaluating the transvalvular pressure gradient, different types of flow oscillation are observed for different valve cases. In the BP-100, BP-M50, and BP-M12.5 cases, small-amplitude oscillations are initially observed in the transvalvular pressure before $t = 0.1$ s and subside after $t = 0.16$ s. In the the BP-F50 and BP-MF50, oscillations in the pressure are observed beginning after $t = 0.05$ s. In these cases, the initial amplitude of the pressure oscillations is relatively small and exhibits a substantial amplification over the $t = 0.1$ to 0.3 s time period, indicative of leaflet flutter in these cases, that is not present in the BP-100, BP-M50, and BP-M12.5 cases. As observed from these results, the cases that have a reduced membrane stiffness also indicate a decrease in the pressure gradient that results from the additional radial expansion or stretching that is allowed for these valves, which will be more apparent

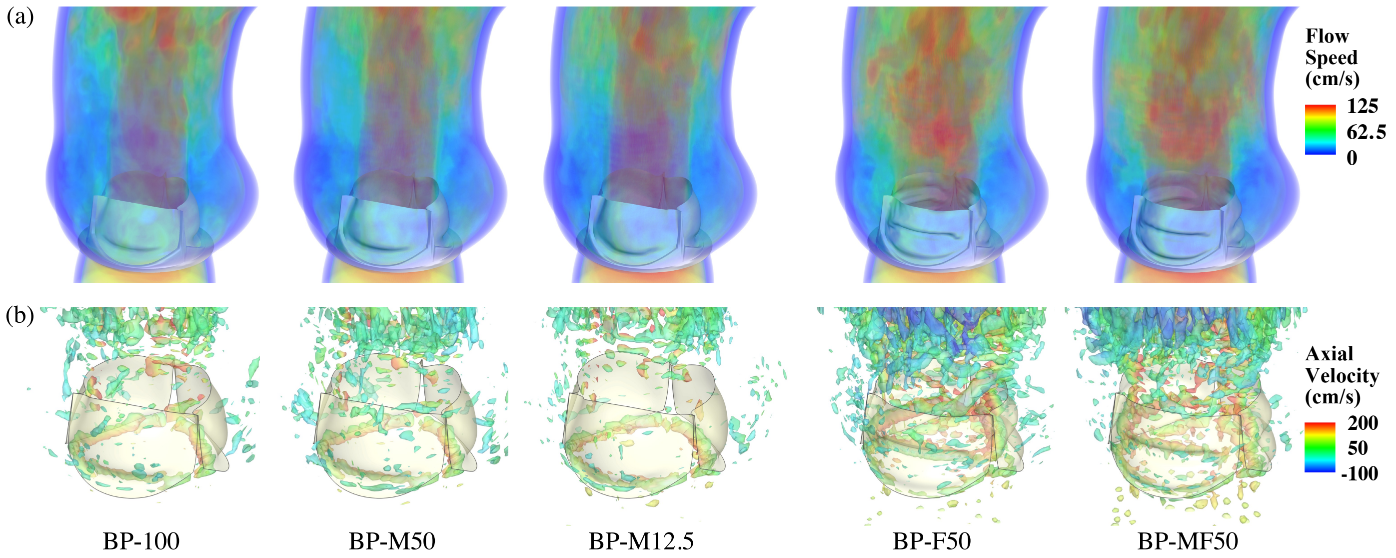

Figure 2: FSI simulation results at $t = 0.25$ s for each valve case. (a) Volume rendering visualization of the flow speeds and (b) vorticity isosurfaces, colored by the axial (normal to the aortic annulus) velocity.

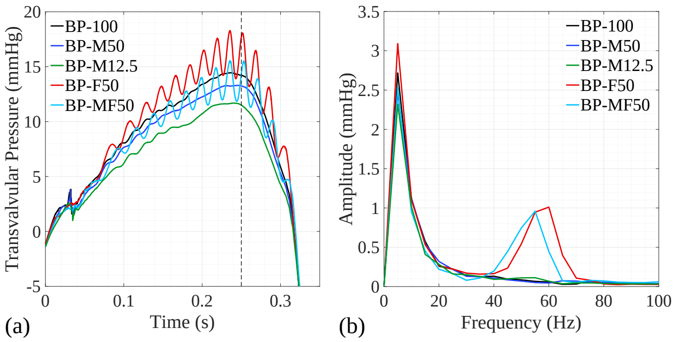

Figure 3: Transvalvular pressure results for each valve case. (a) Transvalvular pressure gradient computed between the left ventricle (0.1 cm below the annulus) and the aorta (1.3 cm above the annulus) and (b) frequency domain from discrete Fourier transform operations for the $t = 0.1$ to 0.3 s time period of the transvalvular pressure signal.

from the geometric orifice area results presented in the following sections.

To specifically examine the prominent high-frequency flow fluctuations within the $t = 0.1$ to 0.3 s time period, we isolate this section of the opening period for further frequency analysis (Fig. 3b). In each case, some low frequencies are present due to the overall opening and closure behavior of the valve within this time period that are also observed in the frequency analysis of the left ventricular pressure waveform in Fig. 1; however, there are also characteristic high frequencies within the 40–70 Hz frequency range for the BP-F50 and BP-MF50 cases. This high-frequency pressure gradient oscillation corresponds to the flutter behavior in these cases, with the BP-F50 valve exhibiting primary high frequencies around 60 Hz and the BP-MF50 valve exhibiting high frequencies near 55 Hz.

3.3. Valve opening area

To obtain a better understanding of the valve behavior, the geometric orifice area (GOA), or anatomical area of the aortic valve orifice, is also quantified. The GOA is calculated by projecting the opening area of the valve onto the plane perpendicular to the aortic axis. Fig. 4 shows the outline of the five valve cases from the top view for selected time instances of $t = 0.23$, 0.24, 0.25, and 0.26 s. The supplementary video also shows the leaflet motion during the $t = 0.0$ to 0.35 time period. These results show the overall valve opening and demonstrate the apparent geometric variation of the free edge during this time period in the BP-F50 and BP-MF50 cases that experience flutter. The projected GOA is also calculated and shown for the opening period ($t = 0$ to 0.35 s) in Fig. 5 and the supplementary video. Frequency analysis of the $t = 0.1$ to 0.3 s time interval is again performed to obtain the frequency-domain behavior of the GOA signal. From the GOA results, it is clear that each case has some degree of oscillation in the initial stage of the valve opening. Based on the overall valve behavior for each case during this opening stage, this oscillation is likely the dynamic response of the leaflet system under the applied pressure load. In the BP-100, BP-M50, and BP-M12.5 cases, this transient response is damped throughout the opening period, as observed from the diminishing oscillation amplitudes in these cases. In the BP-F50 and BP-MF50 cases, some of the same initial oscillations in the GOA signal are observed, likely due to the dynamic response of the leaflets; however, this behavior is not damped over the $t = 0.1$ to 0.3 s time period. Instead, the oscillation behavior is amplified and continues to increase until the valve begins to close. This response indicates significant leaflet flutter in the cases with the reduced flexural stiffness that is not observed with the reduced membrane stiffness. High frequencies corresponding to the high-frequency flutter oscillations are also observed in the frequency domain for these cases.

As observed from the GOA results, reducing the membrane stiffness produces larger valve opening areas. While reducing the flexural stiffness induces a flutter response in the BP-F50 case, this change does not significantly alter the lower-bound value of the GOA compared to the BP-100 case, and the in-

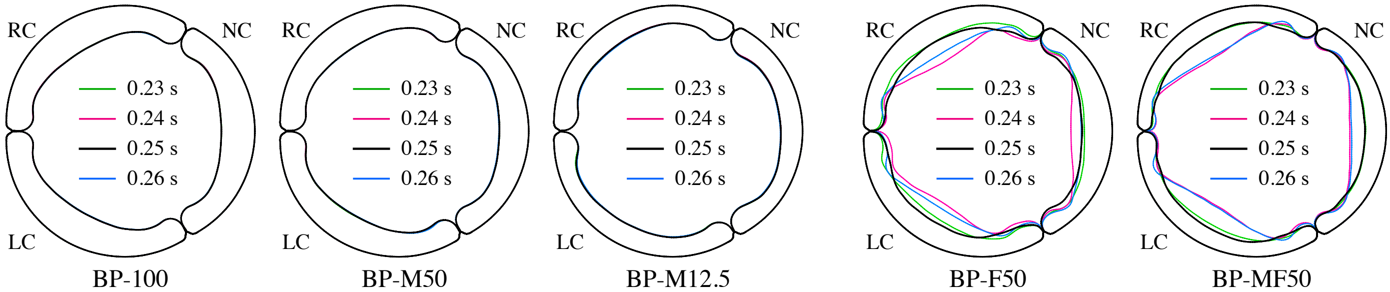

Figure 4: Top view of the leaflet free-edge shapes for each valve case at selected time instances.

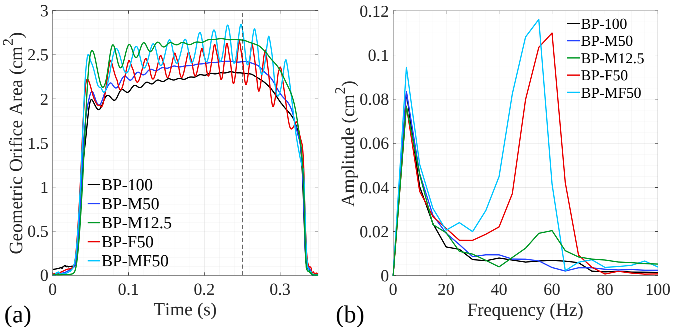

Figure 5: Results from the projected geometric orifice area (GOA) calculation for each valve. (a) Projected GOA for each valve and (b) frequency domain from the discrete Fourier transform operations for t = 0.1 to 0.3 s of the GOA.

Table 2: Energy efficiency (η) of each valve. The energy efficiency is defined as the ratio between flow energy exiting and entering the aorta during one cardiac cycle. ϵ denotes the relative difference with respect to the BP-100 case.

	BP-100	BP-M50	BP-M12.5	BP-F50	BP-MF50
η (%)	90.46	91.61	92.26	89.28	90.31
ϵ (%)	—	1.27	1.99	−1.30	−0.16

crease in area above the BP-100 results is primarily due to the oscillatory flutter behavior that increases the maximum GOA. The combined effect of the reduced membrane and flexural stiffnesses in the BP-MF50 case has a significant impact on the GOA compared to the BP-100 case due to the addition of flutter and the higher stretching behavior of the valve. Similar high frequencies to those present in the transvalvular pressure gradient data are also observed in the GOA for the BP-F50 and BP-MF50 due to the flutter behavior. In the BP-M12.5 case, the GOA signal contains similar prominent frequencies (55–60 Hz) in the oscillatory dynamic response that are also present in the BP-F50 and BP-MF50 cases. This consistent frequency behavior likely indicates that the leaflet flutter is initially induced as a result of the dynamic response of the tissue that is not mitigated in the leaflets with reduced flexural stiffness.

3.4. *Energy efficiency results*

The results for the energy efficiency of each case are also quantified to identify the impact of the individual stiffness contributions. The energy efficiency, η, is defined as the ratio between the energy fluxes out of and into the system [49] and is calculated by integrating the energy fluxes on the outlet and inlet of the aorta over a complete cardiac cycle. As shown in

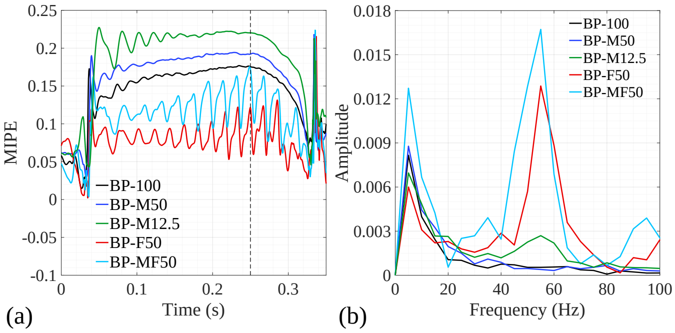

Figure 6: Results from the strain calculation for each valve. (a) Maximum in-plane principal Green–Lagrange strain (MIPE) on the valve evaluated on the aortic side of the shell surface at the center of the free edge of the left coronary leaflet and (b) frequency domain from the discrete Fourier transform operations for t = 0.1 to 0.3 s of the MIPE.

Table 2, the energy efficiency is computed for each case, and the relative change in efficiency in the BP-M50, BP-M12.5, BP-F50, and BP-MF50 cases is compared with the BP-100 case. As observed from these results, the reduced membrane stiffness increases the energy efficiency due to the increased GOA without induced flutter, while the reduced flexural stiffness reduces the energy efficiency due to the introduction of flutter in the BP-F50 and BP-MF50 cases. The combined effect of simultaneously reducing the membrane and flexural stiffnesses leads to a valve that is less efficient than the BP-100 case, due to the flutter behavior, but more efficient than the BP-F50 case due to the increased opening area related to the reduction in the membrane stiffness.

3.5. *Strain results*

The strain on each valve case is also evaluated to identify the impact of the individual stiffness contributions on the structural performance of the valve and the possible contribution to the durability and fatigue behavior of each case. Fig. 6 illustrates the maximum in-plane principal Green–Lagrange strain (MIPE) computed on the aortic side of the shell surface at the center of the free edge of the left coronary leaflet to highlight the temporal strain behavior of the valves. The temporal frequency behavior of the MIPE is also analyzed. The computed quantities for the BP-F50 and BP-MF50 cases again demonstrate the oscillatory motion of the leaflets in time and display frequencies that are similar to the high frequencies that were observed in the GOA, with some additional higher frequencies

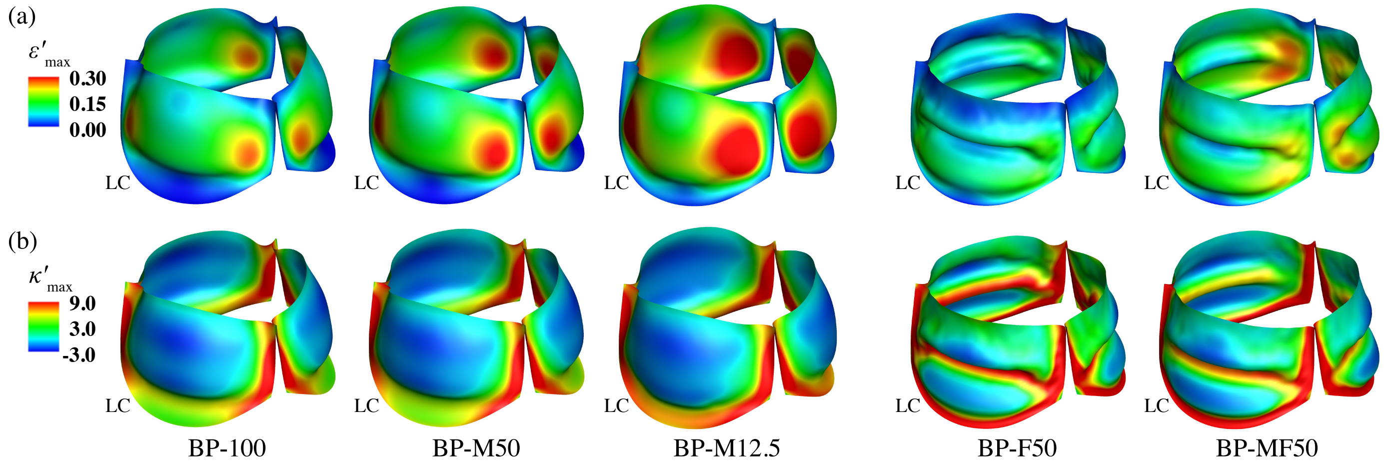

Figure 7: Distributions of the maximum in-plane principal component of the (a) membrane strain tensor $\boldsymbol{\varepsilon}$ and (b) curvature change (due to bending) tensor $\boldsymbol{\kappa}$, denoted as $\varepsilon'_{\max}$ and $\kappa'_{\max}$, respectively, at peak opening (t = 0.25 s). $\varepsilon'_{\max}$ and $\kappa'_{\max}$ are defined and evaluated at the shell midsurface and contribute to the MIPE on the valve. The normal vector of the shell points from the aortic side to the ventricular side of the leaflet.

in the 80–100 Hz range also being observed.

Fig. 7 shows the distributions of the individual contributions of the membrane strain and curvature change (due to bending) to the MIPE for each valve at peak systole. The BP-100 and BP-M50 valves show similar overall behavior in the membrane strain and curvature change distributions; however, the reduction in the membrane stiffness allows the valve to stretch more, resulting in higher membrane strains on the leaflets. The BP-M12.5 case, as expected, also exhibits high membrane strain concentrations centered in similar locations that extend further into different areas of the leaflets compared to the BP-100 and BP-M50 cases. In the cases that do not experience flutter, the highest magnitude and degree of variation in the curvature change is localized near the attachment edges of the leaflets. The central region of each leaflet has a relatively low degree of variation in the curvature change. Despite the flutter behavior in the BP-F50 case, this valve exhibits overall lower membrane strain concentrations due to the minimal stretching in the leaflet compared to the other valves. The BP-MF50 case experiences membrane strains that would be similar to the combined behavior of the BP-M50 and BP-F50 cases. Compared to the valves that do not experience flutter, both the BP-F50 and BP-MF50 valves also exhibit distinctly different overall opening shapes in the leaflets and curvature change distributions due to the higher folding behavior of these valves in the central region of the leaflets. The results for the full MIPE distributions in each case are shown in Appendix C.

4. Discussion

The present study implemented a computational FSI approach to investigate the contributing mechanics in heart valve leaflet flutter for thinner tissues. This work simulated five valve cases, each having different membrane and flexural stiffness properties, to isolate the underlying mechanics that contribute to the initiation of flutter in thinner biological tissues. While leaflet flutter has been previously identified as an undesirable behavior in these valves, due to the possibility of decreased valve durability resulting from increased cyclic stresses [9] and the flutter-induced flow disturbances that may lead an increased risk of thrombosis [12, 50], the primary mechanics contributing to leaflet flutter in thinner tissues had not been previously identified. Based on the results in this study for the specific stiffness quantities and thickness ranges that have been examined, the reduced flexural stiffness is the primary factor that contributes to increased leaflet flutter in the thinner biological tissues, and the membrane stiffness and mass have minimal impacts on the incidence of flutter.

In the cases that experience flutter due to a decreased flexural stiffness corresponding to the thinner tissue, the FSI results indicate disturbed blood flow, oscillatory pressure behavior, and additional induced vortex formation near the valve. The GOA results in the BP-F50 and BP-MF50 cases also exhibit the oscillatory behavior induced by the leaflet flutter in addition to an increased GOA compared to the BP-100 case, with the BP-MF50 valve allowing more valve expansion than the BP-F50 valve due to the decrease in membrane stiffness. In both of these cases, the induced flutter behavior causes a decrease in the energy efficiency due to the increased viscous dissipation. In contrast, while the BP-M50 and BP-M12.5 valves exhibit an increased GOA due to the higher stretching threshold of the tissue, these cases demonstrate an expected increase in energy efficiency when flutter is not present.

The results from the strain signal and distributions also demonstrate the direct changes in leaflet behavior for different cases as well as the induced flutter due to the decreased flexural stiffness corresponding to the reduced tissue thickness in the BP-F50 and BP-MF50 cases. For the strain quantities, these results also indicate the significant increase in maximum strain in the BP-M50 and BP-M12.5 cases due to the reduced membrane stiffness. Although the overall strain in these cases is higher, it is possible that the added localized, high-amplitude cyclic stress in the BP-F50 and BP-MF50 cases could lead to more problematic fatigue behavior compared to overall higher, uniform strain values, particularly if the strain increase is relatively minor (e.g., the BP-M50 case).

While this study focuses on identifying the specific underlying tissue mechanics that contribute to leaflet flutter, there are still a number of limitations in this work and additional flutter-related quantities that could be investigated. The present work explores a finite set of material input parameters that may not capture a comprehensive view of the influence of the properties that were examined in this study. Additionally, the results are for simulations with a single pressure waveform that consider only the specified boundary and pressure conditions. In the future, based on the robustness and flexibility of the IMGA FSI framework for heart valve simulation, additional studies with other conditions, such as different ventricular pressure waveforms or patient-specific conditions, could also be analyzed. Further investigations of the impact of thinner tissues on flutter behavior could explore uncertainty or variation in the experimentally derived parameters or relevant input quantities. Future studies might also investigate the influence of other parameters, such as flow speed and leaflet size [51], as well as geometric variations [52], on leaflet flutter and determine the critical flexural stiffness for the onset of flutter. Extended analysis of flow in the ascending aorta for cases with leaflet flutter could provide additional insight on the physics of turbulence and flutter-induced flow instabilities in the cardiovascular system. Fatigue studies of heart valve leaflet flutter could also improve knowledge about the long-term effects of flutter behavior on the durability of bioprosthetic tissues.

Although there are many possible negative impacts of using thinner biological tissues in heart valve implants, including leaflet flutter, there are also numerous motivating factors to incorporate these tissues in bioprosthetic valves. One of the primary benefits of thinner tissues, particularly in transcatheter valve replacement procedures, is the reduced risk of complications with the smaller-diameter catheters that can be used to deploy implants that incorporate thinner tissues [8]. Additionally, thinner tissues that do not experience flutter can also increase the energy efficiency of the implant by reducing the transvalvular pressure and allowing blood to flow more easily through the aortic valve. Identifying the underlying mechanics that contribute to leaflet flutter provides a clear indication of the mechanical quantities related to thinner tissues that may offer beneficial or detrimental effects. The results from this work offer a substantial opportunity for future research in the area of bioprosthetic tissue engineering for leaflet design. Given the benefits of thinner tissues and the significant impact of the flexural stiffness on leaflet flutter, an ideal bioprosthetic implant would incorporate relatively thin tissues with a low to moderate membrane stiffness and comparatively high flexural stiffness to improve valve performance and simultaneously mitigate flutter behavior and its negative effects.

Appendix A. St. Venant–Kirchhoff material

For the isotropic St. Venant–Kirchhoff material, $\mathbf{S} = \bar{\mathbb{C}}\,\mathbf{E}$, where $\bar{\mathbb{C}}$ is the elasticity tensor that is constant through the shell thickness. For this linear stress–strain relationship, in contrast to general hyperelastic materials, it is relatively straightforward to separate the individual membrane and bending contributions within the internal stiffness. In this model, Eqs. (5), (6), and (12)–(14) become

$$\mathbf{n} = \int_{-h/2}^{h/2} \mathbf{S}\,\mathrm{d}\xi^3 = \int_{-h/2}^{h/2} \bar{\mathbb{C}}\left(\boldsymbol{\varepsilon} + \xi^3 \boldsymbol{\kappa}\right)\mathrm{d}\xi^3 = h\,\bar{\mathbb{C}}\,\boldsymbol{\varepsilon}\,, \tag{A.1}$$

$$\mathbf{m} = \int_{-h/2}^{h/2} \mathbf{S}\,\xi^3 \mathrm{d}\xi^3 = \int_{-h/2}^{h/2} \bar{\mathbb{C}}\left(\boldsymbol{\varepsilon} + \xi^3 \boldsymbol{\kappa}\right)\xi^3 \mathrm{d}\xi^3 = \frac{h^3}{12}\bar{\mathbb{C}}\,\boldsymbol{\kappa}\,, \tag{A.2}$$

$$\mathbb{D}_A = \int_{-h/2}^{h/2} \bar{\mathbb{C}}\,\mathrm{d}\xi^3 = h\,\bar{\mathbb{C}}\,, \tag{A.3}$$

$$\mathbb{D}_B = \int_{-h/2}^{h/2} \bar{\mathbb{C}}\,\xi^3 \mathrm{d}\xi^3 = 0\,, \tag{A.4}$$

$$\mathbb{D}_D = \int_{-h/2}^{h/2} \bar{\mathbb{C}}\left(\xi^3\right)^2 \mathrm{d}\xi^3 = \frac{h^3}{12}\bar{\mathbb{C}}\,, \tag{A.5}$$

and the internal stiffness matrix becomes

$$\begin{aligned} K^{\mathrm{int}}_{rs} = \int_{\mathcal{S}_0} \Bigg(& \mathbb{D}_A \frac{\partial \boldsymbol{\varepsilon}}{\partial u_s} : \frac{\partial \boldsymbol{\varepsilon}}{\partial u_r} + \mathbf{n} : \frac{\partial^2 \boldsymbol{\varepsilon}}{\partial u_r \partial u_s} \\ & + \mathbb{D}_D \frac{\partial \boldsymbol{\kappa}}{\partial u_s} : \frac{\partial \boldsymbol{\kappa}}{\partial u_r} + \mathbf{m} : \frac{\partial^2 \boldsymbol{\kappa}}{\partial u_r \partial u_s} \Bigg) \mathrm{d}\mathcal{S}\,. \end{aligned} \tag{A.6}$$

Within this internal stiffness formulation, the first two terms on the right-hand-side of the equation represent the membrane stiffness, and the latter two terms represent the bending stiffness. The membrane–bending coupling stiffness vanishes since $\mathbb{D}_B = 0$, and there are no additional interdependent stiffness terms.

Appendix B. Mass reduction case

To examine the impact of reduced mass on the initiation of flutter, the BP-M12.5 case is compared to an additional case (BP-MM12.5) where the membrane stiffness and mass are both reduced based on 12.5% of the thickness ($0.125H$ instead of $1.0H$). This case is selected as an extreme example to demonstrate a more severe impact of the reduced mass on the flutter behavior. As shown in Fig. B.1, the results of the GOA in these two cases are very similar, with minimal differences observed in

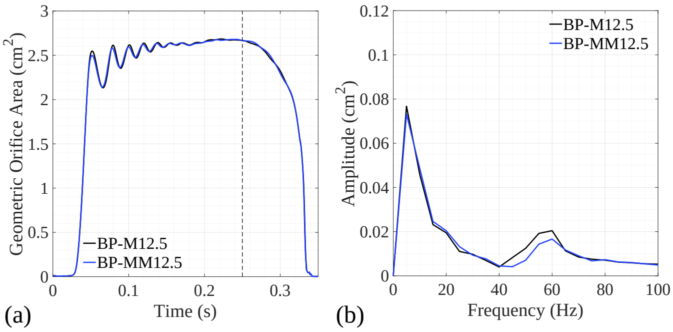

Figure B.1: Results from the projected geometric orifice area (GOA) calculation for the BP-M12.5 and BP-MM12.5 valves. (a) Projected GOA for each valve case and (b) frequency domain from the discrete Fourier transform operations for $t = 0.1$ to 0.3 s of the GOA.

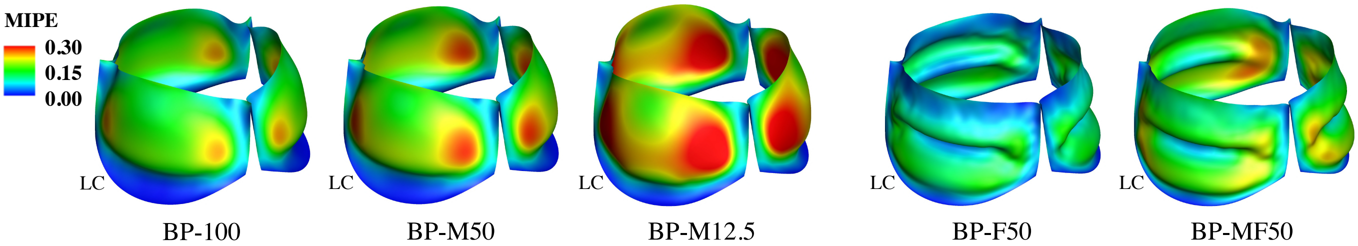

Figure C.1: Maximum in-plane principal Green–Lagrange strain (MIPE) on each valve at the peak opening (t = 0.25 s) evaluated on the aortic side of the leaflets.

the magnitude of the dynamic responses. Even with the significant mass reduction in this case, the dynamic leaflet response is damped out during the opening period, and there is no flutter induced in the BP-MM12.5 case, which indicates that the mass does not significantly impact the flutter behavior of the leaflets.

Appendix C. Green–Lagrange strain distributions

The distributions of the maximum in-plane principal Green–Lagrange strain (MIPE) are shown in Fig. C.1 for the peak opening at $t = 0.25$ s. These results show the combined effect of the membrane strain and the curvature change distributions, shown in Fig. 7. The Green–Lagrange strain ($\mathbf{E}$) is based on Eq. (2) and is evaluated on the aortic side of the leaflets based on the tissue thickness that is used to compute the flexural stiffness, which maintains through-thickness properties that are consistent with the simulation quantities.

Acknowledgments

This work was supported by the National Heart, Lung, and Blood Institute of the National Institutes of Health under award numbers R01HL129077 and R01HL142504. This support is gratefully acknowledged. We thank the Texas Advanced Computing Center (TACC) at The University of Texas at Austin for providing HPC resources that have contributed to the research results reported in this paper.

References

[1] J. S. Soares, K. R. Feaver, W. Zhang, D. Kamensky, A. Aggarwal, and M. S. Sacks. Biomechanical behavior of bioprosthetic heart valve heterograft tissues: Characterization, simulation, and performance. *Cardiovascular Engineering and Technology*, 7(4):309–351, 2016.

[2] M. Arsalan and T. Walther. Durability of prostheses for transcatheter aortic valve implantation. *Nature Reviews Cardiology*, 13:360–367, 2016.

[3] S. Maximus, J. C. Milliken, B. Danielsen, R. Shemin, J. Khan, and J. S. Carey. Implementation of transcatheter aortic valve replacement in California: Influence on aortic valve surgery. *Journal of Thoracic and Cardiovascular Surgery*, 155(4):1447–1456, 2018.

[4] V. T. Nkomo, J. M. Gardin, T. N. Skelton, J. S. Gottdiener, C. G. Scott, and M. Enriquez-Sarano. Burden of valvular heart diseases: a population-based study. *The Lancet*, 368(9540):1005–1011, 2006.

[5] P. Pibarot and J. G. Dumesnil. Prosthetic heart valves: selection of the optimal prosthesis and long-term management. *Circulation*, 119(7):1034–1048, 2009.

[6] R. Guidoin, Y. Douville, M.-A. Clavel, Z. Zhang, M. Nutley, P. Pibarot, and G. Dionne. The marvel of percutaneous cardiovascular devices in the elderly. *Annals of the New York Academy of Sciences*, 1197(1):188–199, 2010.

[7] C. R. Smith, M. B. Leon, M. J. Mack, D. C. Miller, J. W. Moses, L. G. Svensson, E. M. Tuzcu, J. G. Webb, G. P. Fontana, R. R. Makkar, M. Williams, T. Dewey, S. Kapadia, V. Babaliaros, V. H. Thourani, P. Corso, A. D. Pichard, J. E. Bavaria, H. C. Herrmann, J. J. Akin, W. N. Anderson, D. Wang, and S. J. Pocock. Transcatheter versus surgical aortic-valve replacement in high-risk patients. *New England Journal of Medicine*, 364(23):2187–2198, 2011.

[8] A. Caballero, F. Sulejmani, C. Martin, T. Pham, and W. Sun. Evaluation of transcatheter heart valve biomaterials: Biomechanical characterization of bovine and porcine pericardium. *Journal of the Mechanical Behavior of Biomedical Materials*, 75:486–494, 2017.

[9] E. L. Johnson, M. C. H. Wu, F. Xu, N. M. Wiese, M. R. Rajanna, A. J. Herrema, B. Ganapathysubramanian, T. J. R. Hughes, M. S. Sacks, and M.-C. Hsu. Thinner biological tissues induce leaflet flutter in aortic heart valve replacements. *Proceedings of the National Academy of Sciences*, 117(32):19007–19016, 2020.

[10] M. Giersiepen, L. J. Wurzinger, R. Opitz, and H. Reul. Estimation of shear stress-related blood damage in heart valve prostheses - in vitro comparison of 25 aortic valves. *The International Journal of Artificial Organs*, 13(5):300–306, 1990.

[11] H. Nygaard, M. Giersiepen, J. M. Hasenkam, H. Reul, P. K. Paulsen, P. E. Rovsing, and D. Westphal. Two-dimensional color-mapping of turbulent shear stress distribution downstream of two aortic bioprosthetic valves in vitro. *Journal of Biomechanics*, 25(4):429 – 440, 1992.

[12] H. Hatoum, A. Yousefi, S. Lilly, P. Maureira, J. Crestanello, and L. P. Dasi. An in vitro evaluation of turbulence after transcatheter aortic valve implantation. *The Journal of Thoracic and Cardiovascular Surgery*, 156 (5):1837–1848, 2018.

[13] E. R. Pinto, P. M. Damani, C. N. Sternberg, and A. J. Liedtke. Fine flutterings of the aortic valve as demonstrated by aortic valve echocardiograms. *American Heart Journal*, 95(6):807–808, 1978.

[14] W. G. Rainer, R. A. Christopher, T. R. Sadler Jr., and A. D. Hilgenberg. Dynamic behavior of prosthetic aortic tissue valves as viewed by high-speed cinematography. *The Annals of Thoracic Surgery*, 28(3):274–280, 1979.

[15] E. K. Louie, T. J. Mason, R. Shah, T. Bieniarz, and A. M. Moore. Determinants of anterior mitral leaflet fluttering in pure aortic regurgitation from pulsed Doppler study of the early diastolic interaction between the regurgitant jet and mitral inflow. *The American Journal of Cardiology*, 61 (13):1085–1091, 1988.

[16] J. A. Peacock. An in vitro study of the onset of turbulence in the sinus of Valsalva. *Circulation Research*, 67(2):448–460, 1990.

[17] P. Marx, W. Kowalczyk, A. Demircioglu, S.-E. Shehada, H. Wendta, F. Mourad, M. Thielmann, H. Jakob, and D. Wendt. An in vitro comparison of flow dynamics of the Magna Ease and the Trifecta prostheses. *Minimally Invasive Therapy & Allied Technologies*, 29(2):78–85, 2020.

[18] T. Ishihara, V. J. Ferrans, S. W. Boyce, M. Jones, and W. C. Roberts. Structure and classification of cuspal tears and perforations in porcine bioprosthetic cardiac valves implanted in patients. *American Journal of Cardiology*, 48(4):665–678, 1981.

[19] J. L. Pomar, X. Bosch, B. R. Chaitman, C. Pelletier, and C. M. Grondin. Late tears in leaflets of porcine bioprostheses in adults. *The Annals of Thoracic Surgery*, 37(1):78–83, 1984.

[20] R. F. Siddiqui, J. R. Abraham, and J. Butany. Bioprosthetic heart valves: Modes of failure. *Histopathology*, 55:135–144, 2009.

[21] A. Koziarz, A. Makhdoum, J. Butany, M. Ouzounian, and J. Chung. Modes of bioprosthetic valve failure: a narrative review. *Current opinion in cardiology*, 35(2):123–132, 2020.

[22] M. Marro, A P Kossar, Y. Xue, A. Frasca, R. J. Levy, and G. Ferrari. Noncalcific mechanisms of bioprosthetic structural valve degeneration. *Journal of the American Heart Association*, 10(3):e018921, 2021.

[23] J. Kiendl, K.-U. Bletzinger, J. Linhard, and R. Wüchner. Isogeometric shell analysis with Kirchhoff–Love elements. *Computer Methods in Applied Mechanics and Engineering*, 198:3902–3914, 2009.

[24] Y. Chen and H. Luo. Pressure distribution over the leaflets and effect of bending stiffness on fluid–structure interaction of the aortic valve. *Journal of Fluid Mechanics*, 883:A52, 2020.

[25] D. Kamensky, M.-C. Hsu, D. Schillinger, J. A. Evans, A. Aggarwal, Y. Bazilevs, M. S. Sacks, and T. J. R. Hughes. An immersogeometric variational framework for fluid–structure interaction: Application to bioprosthetic heart valves. *Computer Methods in Applied Mechanics and Engineering*, 284:1005–1053, 2015.

[26] M.-C. Hsu and D. Kamensky. Immersogeometric analysis of bioprosthetic heart valves, using the dynamic augmented Lagrangian method. In T. E. Tezduyar, editor, *Frontiers in Computational Fluid–Structure Interaction and Flow Simulation*, pages 167–212. Springer International Publishing, Cham, 2018.

[27] M.-C. Hsu, D. Kamensky, Y. Bazilevs, M. S. Sacks, and T. J. R. Hughes. Fluid–structure interaction analysis of bioprosthetic heart valves: significance of arterial wall deformation. *Computational Mechanics*, 54(4): 1055–1071, 2014.

[28] M.-C. Hsu, D. Kamensky, F. Xu, J. Kiendl, C. Wang, M. C. H. Wu, J. Mineroff, A. Reali, Y. Bazilevs, and M. S. Sacks. Dynamic and fluid–structure interaction simulations of bioprosthetic heart valves using parametric design with T-splines and Fung-type material models. *Computational Mechanics*, 55:1211–1225, 2015.

[29] D. Kamensky, J. A. Evans, and M.-C. Hsu. Stability and conservation properties of collocated constraints in immersogeometric fluid–thin structure interaction analysis. *Communications in Computational Physics*, 18: 1147–1180, 2015.

[30] F. Xu, S. Morganti, R. Zakerzadeh, D. Kamensky, F. Auricchio, A. Reali, T. J. R. Hughes, M. S. Sacks, and M.-C. Hsu. A framework for designing patient-specific bioprosthetic heart valves using immersogeometric fluid–structure interaction analysis. *International Journal for Numerical Methods in Biomedical Engineering*, 34(4):e2938, 2018.

[31] Y. Yu, D. Kamensky, M.-C. Hsu, X. Y. Lu, Y. Bazilevs, and T. J. R. Hughes. Error estimates for projection-based dynamic augmented Lagrangian boundary condition enforcement, with application to fluid–structure interaction. *Mathematical Models and Methods in Applied Sciences*, 28(12):2457–2509, 2018.

[32] M. C. H. Wu, H. M. Muchowski, E. L. Johnson, M. R. Rajanna, and M.-C. Hsu. Immersogeometric fluid–structure interaction modeling and simulation of transcatheter aortic valve replacement. *Computer Methods in Applied Mechanics and Engineering*, 357:112556, 2019.

[33] F. Xu, E. L. Johnson, C. Wang, A. Jafari, C.-H. Yang, M. S. Sacks, A. Krishnamurthy, and M.-C. Hsu. Computational investigation of left ventricular hemodynamics following bioprosthetic aortic and mitral valve replacement. *Mechanics Research Communications*, 112:103604, 2021.

[34] K. Takizawa, Y. Bazilevs, and T. E. Tezduyar. Space–time and ALE-VMS techniques for patient-specific cardiovascular fluid–structure interaction modeling. *Archives of Computational Methods in Engineering*, 19:171–225, 2012.

[35] T. Terahara, K. Takizawa, T. E. Tezduyar, Y. Bazilevs, and M.-C. Hsu. Heart valve isogeometric sequentially-coupled FSI analysis with the space–time topology change method. *Computational Mechanics*, 65: 1167–1187, 2020.

[36] B. E. Griffith, X. Luo, D. M. McQueen, and C. S. Peskin. Simulating the fluid dynamics of natural and prosthetic heart valves using the immersed boundary method. *International Journal of Applied Mechanics*, 01:137–177, 2009.

[37] T. J. R. Hughes, L. Mazzei, and K. E. Jansen. Large eddy simulation and the variational multiscale method. *Computing and Visualization in Science*, 3:47–59, 2000.

[38] Y. Bazilevs, V. M. Calo, J. A. Cottrel, T. J. R. Hughes, A. Reali, and G. Scovazzi. Variational multiscale residual-based turbulence modeling for large eddy simulation of incompressible flows. *Computer Methods in Applied Mechanics and Engineering*, 197:173–201, 2007.

[39] K. Takizawa, Y. Bazilevs, T. E. Tezduyar, C. C. Long, A. L. Marsden, and K. Schjodt. ST and ALE-VMS methods for patient-specific cardiovascular fluid mechanics modeling. *Mathematical Models and Methods in Applied Sciences*, 24:2437–2486, 2014.

[40] T. J. R. Hughes, W. K. Liu, and T. K. Zimmermann. Lagrangian–Eulerian finite element formulation for incompressible viscous flows. *Computer Methods in Applied Mechanics and Engineering*, 29:329–349, 1981.

[41] Y. Bazilevs, V. M. Calo, T. J. R. Hughes, and Y. Zhang. Isogeometric fluid–structure interaction: theory, algorithms, and computations. *Computational Mechanics*, 43:3–37, 2008.

[42] J. Kiendl, M.-C. Hsu, M. C. H. Wu, and A. Reali. Isogeometric Kirchhoff–Love shell formulations for general hyperelastic materials. *Computer Methods in Applied Mechanics and Engineering*, 291:280–303, 2015.

[43] M. C. H. Wu, R. Zakerzadeh, D. Kamensky, J. Kiendl, M. S. Sacks, and M.-C. Hsu. An anisotropic constitutive model for immersogeometric fluid–structure interaction analysis of bioprosthetic heart valves. *Journal of Biomechanics*, 74:23–31, 2018.

[44] I. E. Vignon-Clementel, C. A. Figueroa, K. E. Jansen, and C. A. Taylor. Outflow boundary conditions for three-dimensional finite element modeling of blood flow and pressure in arteries. *Computer Methods in Applied Mechanics and Engineering*, 195:3776–3796, 2006.

[45] M. Esmaily-Moghadam, Y. Bazilevs, T.-Y. Hsia, I. E. Vignon-Clementel, A. L. Marsden, and Modeling of Congenital Hearts Alliance (MOCHA). A comparison of outlet boundary treatments for prevention of backflow divergence with relevance to blood flow simulations. *Computational Mechanics*, 48:277–291, 2011.

[46] J. C. Simo and T. J. R. Hughes. *Computational Inelasticity*. Springer-Verlag, New York, 1998.

[47] Y. Bazilevs, M.-C. Hsu, Y. Zhang, W. Wang, T. Kvamsdal, S. Hentschel, and J. Isaksen. Computational fluid–structure interaction: Methods and application to cerebral aneurysms. *Biomechanics and Modeling in Mechanobiology*, 9:481–498, 2010.

[48] W. Sun and M. S. Sacks. Finite element implementation of a generalized Fung-elastic constitutive model for planar soft tissues. *Biomechanics and Modeling in Mechanobiology*, 4:190–199, 2005.

[49] A. L. Marsden, I. E. Vignon-Clementel, F. Chan, J. A. Feinstein, and C. A. Taylor. Effects of exercise and respiration on hemodynamic efficiency in CFD simulations of the total cavopulmonary connection. *Annals of Biomedical Engineering*, 35:250–263, 2007.

[50] R. L. Smith, E. F. Blick, J. Coalson, and P. D. Stein. Thrombus production by turbulence. *Journal of Applied Physiology*, 32(2):261–264, 1972.

[51] J. H. Lee, L. N. Scotten, R. Hunt, T. G. Caranasos, J. P. Vavalle, and B. E. Griffith. Bioprosthetic aortic valve diameter and thickness are directly related to leaflet fluttering: Results from a combined experimental and computational modeling study. *JTCVS Open*, 6:60–81, 2021.

[52] E. L. Johnson, D. W. Laurence, F. Xu, C. E. Crisp, A. Mir, H. M. Burkhart, C.-H. Lee, and M.-C. Hsu. Parameterization, geometric modeling, and isogeometric analysis of tricuspid valves. *Computer Methods in Applied Mechanics and Engineering*, 384:113960, 2021.